



1

2 **Development of an OMI AI data assimilation scheme for aerosol modeling over bright  
3 surfaces—a step toward direct radiance assimilation in the UV spectrum**

4

5 Jianglong Zhang<sup>1</sup>, Robert J. D. Spurr<sup>2</sup>, Jeffrey S. Reid<sup>3</sup>, Peng Xian<sup>3</sup>, Peter R. Colarco<sup>4</sup>, James R.  
6 Campbell<sup>3</sup>, Edward J. Hyer<sup>3</sup>, and Nancy Baker<sup>3</sup>

7

8 <sup>1</sup>Department of Atmospheric Sciences, University of North Dakota, Grand Forks, ND

9 <sup>2</sup>RT SOLUTIONS Inc., Cambridge MA

10 <sup>3</sup>Marine Meteorology Division, Naval Research Laboratory, Monterey, CA

11 <sup>4</sup>NASA Goddard Space Flight Center, Greenbelt, MD

12

13

14

15

16 Submitted to

17 GMD

18

19

20 June 2020

21

22

23

24

25 Corresponding Author: [jianglong.zhang@und.edu](mailto:jianglong.zhang@und.edu)



26

## Abstract

27 Using the Vector LInearized Discrete Ordinate Radiative Transfer (VLIDORT) code as the main  
28 driver for forward model simulations, a first-of-its-kind data assimilation scheme has been  
29 developed for assimilating Ozone Monitoring Instrument (OMI) aerosol index (AI) measurements  
30 into the Naval Aerosol Analysis and Predictive System (NAAPS). This study suggests both RMSE  
31 and absolute errors can be significantly reduced in NAAPS analyses with the use of OMI AI data  
32 assimilation, when compared to values from NAAPS natural runs. Improvements in model  
33 simulations demonstrate the utility of OMI AI data assimilation for improving the accuracy of  
34 aerosol model analysis over cloudy regions and bright surfaces. However, the OMI AI data  
35 assimilation alone does not out-perform aerosol data assimilation that uses passive-based aerosol  
36 optical depth (AOD) products over cloud free skies and dark surfaces. Further, as AI assimilation  
37 requires the deployment of a fully-multiple-scatter-aware radiative transfer model in the forward  
38 simulations, computational burden is an issue. Nevertheless, the newly-developed modeling  
39 system contains the necessary ingredients for assimilation of radiances in the ultra-violet (UV)  
40 spectrum, and our study shows the potential of direct radiance assimilation at both UV and visible  
41 spectrums, possibly coupled with AOD assimilation, for aerosol applications in the future.  
42 Additional data streams can be added, including data from TROPOspheric Monitoring Instrument  
43 (TROPOMI), Ozone Mapping and Profiler Suite (OMPS) and eventually with the Plankton,  
44 Aerosol, Cloud and ocean Ecosystem (PACE) mission.

45

46



47 **1.0 Introduction**

48 Operational chemical transport modeling (CTM) of atmospheric aerosol particles,  
49 including simulation of sources and sinks and long-range transport of aerosol events such as  
50 biomass burning aerosols from fires and dust outbreaks, is now commonplace at global  
51 meteorology centers for air quality and visibility forecasts (e.g. Sessions et al., 2015; Lynch et al.,  
52 2016). Variational and ensemble-based assimilation of satellite derived aerosol products such as  
53 aerosol optical depth (AOD), lidar backscatter measurements, and surface aerosol properties, can  
54 substantially improve accuracies in CTM analyses and forecasts (Zhang et al., 2008; 2011; 2014;  
55 Yumimoto et al., 2008; Uno et al., 2008; Benedetti et al., 2009; Schutgens et al., 2010; Sekiyama  
56 et al., 2010; Saide et al. 2013; Schwartz, 2012; Li et al., 2013; Rubin et al., 2017; Lynch et al.,  
57 2016).

58 Currently, the main satellite inputs for operational aerosol modeling are AOD products  
59 derived from passive-based polar orbiting imagers, such as the Moderate Resolution Imaging  
60 Spectroradiometer (MODIS), the Visible Infrared Imaging Radiometer Suite (VIIRS), and the  
61 Advance Very High Resolution Radiometer (AVHRR). Experimentation is proceeding with the  
62 use of products from the multi-angle imaging spectroradiometer (MISR) (e.g., Lynch et al., 2016;  
63 Randles et al. 2017; Buchard et al. 2017) and from geostationary instruments such as Himawari  
64 and Geostationary Operational Environmental Satellite (GOES). A major advantage with such  
65 passive-based satellite sensors is that the AOD is retrieved with high spatial and temporal  
66 resolutions over relatively broad fields-of-view (e.g. Zhang et al., 2014). For example, MODIS  
67 and VIIRS provide near-global daily daytime coverage (e.g. Levy et al., 2013; Hsu et al., 2019)  
68 and GOES and Himawari are capable of retrieving AOD over North American and East Asia  
69 regions at sub-hourly temporal resolution (e.g. Bessho et al., 2016).



70 To date, these traditional passive-based satellite AOD retrievals have been limited to darker  
71 surfaces and relatively cloud-free conditions. The widely-used MODIS Dark Target aerosol data,  
72 for instance, are available globally over only oceans and dark land surfaces (e.g. Levy et al., 2013).  
73 The MISR and MODIS Deep Blue aerosol products are also available over some arid  
74 environments, but are not applicable to snow and ice covered regions (e.g. Kahn et al., 2010; Hsu  
75 et al., 2013). Also, none of the above-mentioned aerosol products are valid over cloudy regions.

76 In comparison to AOD, the semi-quantitative UV-based aerosol index (AI) has long been  
77 used to monitor major aerosol events such as smoke plumes and dust storms, starting with the  
78 Total Ozone Mapping Spectrometer (TOMS) from the late 1970s (Herman et al., 1997). AI is  
79 derived using the ratio of observed UV radiances to simulated ones assuming only a clear Rayleigh  
80 sky (e.g. Torres et al., 2007). AI retrievals are currently computed using observations from sensors  
81 with ozone-sensitive channels. For example, the Ozone Monitoring Instrument (OMI), Ozone  
82 Mapping and Profiler Suite (OMPS), TROPOspheric Monitoring Instrument (TROPOMI) and the  
83 future Plankton, Aerosol, Cloud and ocean Ecosystem (PACE) mission can detect UV-absorbing  
84 aerosol particles, such as black carbon laden smoke or iron-bearing dust, over bright surfaces, such  
85 as desert, snow and ice covered regions, and aerosol plumes above clouds (e.g. Torres et al., 2012;  
86 Yu et al., 2012; Alfaro-Contreras et al., 2014; 2016).

87 To complement existing AOD assimilating systems, we have developed an AI data  
88 assimilation (AI-DA) system that is capable of assimilating OMI AI over bright surfaces and  
89 cloudy regions for aerosol analyses and forecasts. This study can be considered as one of the first  
90 attempts for direct radiance assimilation in the UV spectrum for aerosol applications, as AI can be  
91 directly computed from UV radiances and the developed OMI AI-DA system has all necessary  
92 components for a typical radiance assimilation package. In time we expect our assimilation model



93 to merge with AOD or solar radiance assimilation to influence aerosol loading, height and  
94 absorption (e.g., VIIRS+OMPS product; such as Lee et al. 2015). Details of the developed OMI  
95 AI assimilation system are presented in the paper, which is organized as follows: Data sets used  
96 in the study are summarized in Section 2; Section 3 discusses the components of the AI-DA  
97 system. Section 4 provides an evaluation of the developed system; and Section 5 contains a  
98 summary discussion.

99

100 **2.0 Datasets and Models**

101 Three datasets are used in this study. These are: (i) the OMI level 2 UV aerosol product  
102 (OMAERUV; Torres et al., 2007), (ii) the Aerosol Robotic Network (AERONET; Holben et al.,  
103 1998) AOD product, and (iii) reanalysis data from the Naval Aerosol Analysis and Prediction  
104 System (NAAPS; Lynch et al., 2016), which was the first operational global aerosol mass transport  
105 model available to the community. The assimilation system is based on spatial and temporal  
106 variations of aerosol particles from NAAPS (Zhang et al., 2006; 2008), and the Vector LInearized  
107 Discrete Ordinate Radiative Transfer (VLIDORT; Spurr, 2006) code is used to construct a forward  
108 model for the AI-DA system.

109

110 **2.1 OMI aerosol product**

111 UV Aerosol Index data from the OMI level 2 version 3 UV aerosol products (OMAERUV)  
112 are used in this study. The OMI instrument is on board the Aura satellite (launched in 2004) and  
113 it observes the earth's atmosphere over the UV/visible spectrum with a pixel size of 13x24 km at  
114 nadir for the global scan mode, and a swath of ~2600 km (Levlett et al., 2018). The daytime  
115 equatorial crossing for the Aura platform is ~1:30 p.m. The dataset comprises the UV AI, viewing



116 and solar geometries, spectrally-dependent surface albedos at the 354 and 388 nm spectral  
117 channels, terrain pressure, geolocations, x-track and algorithm quality flags, plus other aerosol and  
118 ancillary parameters. The UV AI is designed to detect UV-absorbing aerosol particles, and is  
119 based on radiance observations at 354 nm ( $I_{obs354}$ ) and calculated radiance ( $I_{cal354}$ ) at 354 nm for a  
120 Rayleigh (no aerosol) atmosphere (e.g. Torres et al., 2007) as defined as

121 
$$AI = -100 \log_{10} \frac{I_{obs354}}{I_{cal354}}. \quad (1)$$

122 Unbiased, noise-reduced, quality-assured AI data are necessary for AI data assimilation.  
123 This is especially important for OMI observations, due to this particular sensor suffering from the  
124 well-referenced “row anomalies” issues (Torres et al., 2018). To remove pixels with row  
125 anomalies, only retrievals with x-track flag values of 0 are retained. Also, abnormal AI values  
126 were identified over mountain regions. Thus, retrievals with terrain/surface pressure less than 850  
127 hpa are excluded in the study. Finally, only retrievals with OMI AI values larger than -2 are used.  
128 Therefore, OMI observations over cloudy skies, which could have negative OMI AI values, are  
129 also included.

130 Both cloud-free and above-cloud AI data satisfying these quality checks are aggregated /  
131 averaged in  $1 \times 1^\circ$  (Latitude/Longitude) bins. As a radiative transfer model run is applied for each  
132 observation, the gridded data are used in the assimilation process in order to reduce the  
133 computational burden. Averaged parameters for the gridded data include the solar and sensor  
134 zenith angles, the relative azimuth angles, the spectrally-dependent surface albedos at 354 and 388  
135 nm, the cloud fraction, and the AI values themselves. Additional quality assurance steps are also  
136 applied during the spatial-averaging process. Isolated high AI values are removed as follows.  
137 First, for a  $4 \times 4$  pixel box, if the mean AI is less than 0.7 but an individual AI value is larger than



138 0.7, then that one value is removed. Second, if the standard deviation of AI values for a 3x3 pixel  
139 box surrounding a pixel is larger than 0.5, that individual AI value is likewise removed.

140

## 141 **2.2 AERONET data**

142 Version 3 level 2 daytime, cloud-cleared and quality-assured AERONET data are used to  
143 evaluate the performance of the OMI AI data assimilation in our study (Holben et al., 1998; Giles  
144 et al., 2019). During daytime, AOD from AERONET instruments are derived by measuring the  
145 attenuated solar radiance typically at seven wavelengths ranging from 340 to 1020 nm. In this  
146 study, AERONET data are collocated with NAAPS analyses with and without OMI AI  
147 assimilation. In order to collocate AERONET and NAAPS AOD data, AEROENT AOD values  
148 within  $\pm 30$  minutes of a given NAAPS analysis time are averaged and used as ground-based AOD  
149 values for the NAAPS  $1 \times 1^\circ$  (Latitude/Longitude) collocated bins. As AERONET data require a  
150 cloud-free line of sight to the solar disk, the performance of OMI AI data assimilation over overcast  
151 regions is not evaluated.

152

## 153 **2.3 NAAPS and NAAPS reanalysis data**

154 The NAAPS (<http://www.nrlmry.navy.mil/aerosol/>) model is a multi-species, three-  
155 dimensional, Eulerian global transport model using operational Navy Global Environmental  
156 Model (NAVGEN) as the meteorological driver (Hogan et al., 2014). NAAPS provides 6-day  
157 forecasts at a 3-hour interval with a spatial resolution of  $1/3^\circ$  (latitude/Longitude) and 42 vertical  
158 levels on a global scale. NAAPS predicts four aerosol particle classes: anthropogenic and biogenic  
159 fine particles (ABF, such as primary and secondary organic aerosols and sulfate aerosols); dust,  
160 biomass burning smoke; and sea salt (Lynch et al., 2016).



161        The 2003-2018 NAAPS reanalysis version 1 (v1) (Lynch et al., 2016) is a modified version  
162        of the operational NAAPS model. In this version, quality-controlled retrievals of AOD from  
163        MODIS and MISR (Zhang et al., 2006; Hyer et al., 2011; Shi et al., 2014) are assimilated into  
164        NAAPS through the Naval Research Laboratory Atmospheric Variation Data Assimilation  
165        System-AOD system (NAVDAS-AOD; e.g., Zhang et al., 2008; Zhang et al., 2011; Zhang et al.,  
166        2014). Aerosol source functions, including biomass burning, smoke and dust emissions, are tuned  
167        regionally based on the AERONET data. Other aerosol processes, including dry deposition over  
168        water, are also tuned based on AOD data assimilation correction fields. NOAA Climate Prediction  
169        Center (CPC) MORPHing (CMORPH) precipitation data are used to constraint the wet removal  
170        process within the tropics (Joyce et al., 2004). The usage of CMORPH avoids the ubiquitous  
171        precipitation bias that exists in all global atmospheric models (e.g. Dai, 2006) and is proven to  
172        improve aerosol wet deposition, therefore yielding better AOD (Xian et al., 2009). The reanalysis  
173        agrees reasonably well with AERONET data on a global scale (Lynch et al., 2016) and also  
174        reproduces AOD trends that are in a good agreement with satellite based analysis (e.g., Zhang and  
175        Reid, 2010; Hsu et al., 2012). In this study, we use a free running version of NAAPS reanalysis v1  
176        without AOD assimilation to provide aerosol fields every 6 hours at  $1^\circ \times 1^\circ$  (Latitude/Longitude)  
177        resolution.

178

#### 179        **2.4 VLIDORT radiative transfer code**

180        VLIDORT is a linearized, multiple-scatter radiative transfer model for the simultaneous  
181        generation of Stokes 4-vectors and analytically-derived Jacobians (weighting functions) of these  
182        4-vectors with respect to any atmospheric or surface property (Spurr, 2006). The model uses  
183        discrete-ordinate methods to solve the polarized plane-parallel RT equations in a multi-layer



184 atmosphere, plus the solution of a boundary value problem and subsequent source-function  
185 integration to obtain radiation fields at any geometry and any atmospheric level. VLIDORT has a  
186 “pseudo-spherical” *ansatz*: the treatment of solar-beam attenuation in a spherical-shell atmosphere  
187 before scattering. Single-scattering in VLIDORT is accurate for both line-of-sight and solar-beam  
188 spherical geometry. The model has a full thermal emission capability. VLIDORT has two  
189 supplements, one dealing with bidirectional (non-Lambertian) reflection at the surface, and the  
190 other with the inclusion of surface light sources (SIF or water-leaving radiances). Full details on  
191 the VLIDORT model may be found in a recent review paper (Spurr and Christi, 2019, and  
192 references to VLIDORT therein).

193 VLIDORT is used to simulate the AI in this study. Simulations at 354 and 388 nm are  
194 performed both for Rayleigh atmospheres, and for scenarios with aerosol loadings (four mass-  
195 mixing profiles for different aerosol types) taken from the NAAPS model. In addition to the AI,  
196 Jacobian calculations are needed with respect to these aerosol profiles. Firstly, radiance Jacobians  
197 with respect to these four mass-mixing profiles are computed analytically using VLIDORT’s  
198 linearization facility, and secondly the associated Jacobians of AI are further derived through a  
199 second VLIDORT linearization with respect to the Lambertian-equivalent reflectivity. The details  
200 of this process is given in the next section

201

### 202 **3.0 OMI AI assimilation system**

203 The OMI assimilation system has three components: a forward model, a 3-D variational  
204 assimilation system, and a post-processing system. Based on the background NAAPS 3-D aerosol  
205 concentrations for dust, smoke, ABF, and sea salt aerosols, the forward model not only computes  
206 the associated AI values, but also their Jacobians of AI with respect to the four aerosol mass-



207 loading profiles. The 3-D variational assimilation system is a modified 3-D AOD system (Zhang  
208 et al., 2008; 2011; 2014) that computes increments for dust and smoke aerosol concentrations  
209 based on OMI AI data. The post-processing system constructs a new NAAPS analysis based on  
210 the background NAAPS aerosol concentrations and increments as derived from the 3-D variational  
211 assimilation system. Details of the forward model and the modified NAVDAS-AOD system are  
212 described in this section.

213

214 **3.1 Forward model for simulating OMI AI**

215 To construct an AI-DA system, a forward model is needed to simulate AI using aerosol  
216 concentrations from NAAPS. In this study, the forward model is built around the VLIDORT  
217 model, following a similar method to that suggested in Buchard et al. (2015). Here VLIDORT is  
218 configured to compute OMI radiances and Jacobians as functions of the observational conditions  
219 at 354 and 388 nm, using geolocation information from OMI data such as satellite zenith, solar  
220 zenith and relative azimuth angles, as well as ancillary OMI data (surface albedos at 354 and 388  
221 nm).

222 To convert from NAAPS mass-loading concentrations to aerosol extinction and scattering  
223 profiles, we require aerosol optical properties for the four species at 354 and 388 nm, which are  
224 summarized in Table 1. The optical properties of ABF (assumed to be sulfate in this study), sea  
225 salt, dust and smoke aerosols, including mass extinction cross sections and single scattering  
226 albedos at 354 and 388 nm are adapted from NASA's Goddard Earth Observing System version 5  
227 (GEOS-5) model (e.g. Colarco et al., 2014; Buchard et al., 2015). Note that the study period is  
228 July and August of 2007 over Africa, coinciding with the early biomass burning season associated  
229 with lower single scattering albedo values (Eck et al., 2013). With that in mind, we choose a quite



230 low value of 0.85 for the single-scattering albedo value at 354nm (e.g. Eck et al., 2013; Cochrane  
231 et al., 2019). A slightly higher single scattering albedo of 0.86 is assumed at 388 nm. The slight  
232 increase in single scattering albedo from 354 to 388 nm has also been observed from Solar Spectral  
233 Flux Radiometer (SSFR) observations during the recent NASA ObseRvations of CLouds above  
234 Aerosols and their intEractiOnS (ORACLES) Campaign (Pistone et al., 2019). Scattering matrices  
235 for dust, smoke, sea salt and sulfate (to represent ABF) aerosols are based on associated expansion  
236 coefficients (e.g. Colarco et al., 2014; Buchard et al., 2015) taken from NASA's GEOS-5 model.  
237 Also to reduce computational expenses, scalar radiative transfer calculations are performed.

238 To simulate OMI AI, the Lambertian Equivalent Reflectivity (LER) at 388 nm ( $R_{388}$ ) is  
239 needed for estimating LER at 354 nm. The  $R_{388}$  is calculated from VLIDORT, based on equation  
240 2 below, adapted from Buchard et al. (2015), or

$$241 R_{388} = \frac{I_{aer388}(\rho_{388}) - I_{ray388}(0)}{T + S_b(I_{aer388}(\rho_{388}) - I_{ray388}(0))} . \quad (2)$$

242  $I_{ray388}(0)$  is the calculated path radiance at 388 nm assuming a Rayleigh atmosphere with surface  
243 albedo 0.  $T$  and  $S_b$  are the calculated transmittance and spherical albedo at 388 nm.  $I_{aer388}(\rho_{388})$  is  
244 the computed radiance including 3-D aerosol fields from NAAPS and the 388 nm surface albedo  
245 from OMI data. In Buchard et al. (2015), an adjusting factor is applied to  $R_{388}$  by adding the  
246 difference between climatological surface albedos at 354 and 388 nm. The similar approach is  
247 also adopted in this study, as shown in their Equation 3.

$$248 R'_{388} = R_{388} - (\rho_{388} - \rho_{354}) . \quad (3)$$

249 Here,  $R'_{388}$  is surface albedo adjusted Lambertian Equivalent Reflectivity at 388 nm.  $\rho_{388}$  and  $\rho_{354}$   
250 are surface albedo values at 388 and 354 nm channels that are obtained from the OMI OMAERUV  
251 data. Finally, the simulated AI ( $AI_{naaps}$ ) is given by

$$252 AI_{naaps} = -100 \log_{10} \frac{I_{aer354}(\rho_{354})}{I_{ray354}(R'_{388})} . \quad (4)$$



253 Here,  $I_{aer354}(\rho_{354})$  is the calculated radiance at 354 nm using NAAPS aerosol fields as well as the  
254 OMI-reported surface albedo at 354 nm ( $\rho_{354}$ ).  $I_{ray354}(R_{388})$  is the calculated radiance assuming a  
255 Rayleigh atmosphere and the derived value of  $R_{388}$  as surface albedo (Buchard et al., 2015).

256 The forward model-simulated OMI AI values are inter-compared with OMI AI values as  
257 shown in Figure 1 for the study region. A total of one month (01-31 July 2007) of NAAPS  
258 reanalysis data and OMI AI data were used. Note that OMI AI data over both cloud-free and  
259 cloudy skies were used. Since surface albedos included in the OMI data represent reflectivities  
260 under clear-sky situations, the albedo under cloudy sky is then computed

261 
$$\rho_{cld} = \rho_{clr} * (1 - f_c) + 0.8 * f_c \quad . \quad (5)$$

262 Here,  $\rho_{clr}$  and  $f_c$  are the clear sky surface albedo (e.g.  $\rho_{354}$  or  $\rho_{388}$ ) and the cloud fraction, both  
263 quantities obtained from the OMI dataset. Clouds are assumed to be tropospheric (close to the  
264 surface) with an UV albedo of 0.8, such that this equation applies to both the 354 and 388 nm  
265 channels.

266 Figure 1a shows the spatial distribution of NAAPS AOD over Central and North Africa,  
267 using collocated NAAPS and OMI AI datasets. OMI AI data are grid-averaged in  $1^\circ \times 1^\circ$   
268 (latitude/longitude) bins. Also, we focus over Africa in this paper as this area includes dust plumes  
269 over deserts and smoke plumes overlying stratus cloud decks. The Arctic is not included as  
270 additional efforts may be needed to fully understand properties of sea ice reflectivity; we leave this  
271 topic for a future paper. Only bins that have valid NAAPS and OMI AI data are used to generate  
272 Figure 1. Dust plumes are visible over North Africa and the Persian Gulf, and a smoke plume from  
273 Central Africa is also evident. These UV-absorbing aerosol plumes are also captured by OMI AI,  
274 as seen in Figure 1c. Shown in Figure 1b are the simulated OMI AI using the NAAPS aerosol  
275 fields and viewing geometries and surface albedos from OMI. The simulated OMI AI shows



276 similar patterns to those derived from OMI, especially for the dust plumes over North Africa and  
277 smoke plumes over Central Africa. An overall correlation of 0.785 is found between simulated  
278 and satellite-retrieved OMI AI values, as shown in Figure 1, suggesting the forward model is  
279 functioning reasonably as designed.

280

### 281 3.1 Forward model for Jacobians of AI

282 Jacobians of OMI AI with respect to aerosol mass concentrations are needed for the OMI  
283 AI assimilation system. In this study, AI Jacobians (K) are calculated from radiance Jacobians  
284 with respect to aerosol mass concentrations for four aerosol species (smoke, dust, ABF/sulfate,  
285 sea-salt) at 354 nm ( $K_{354,nk} = \frac{\partial I_{aer354}}{\partial M_{nk}}$ ) and 388 nm ( $K_{388,nk} = \frac{\partial I_{aer388}}{\partial M_{nk}}$ ) wavelengths. Here  $M_{nk}$   
286 is the mass concentration for aerosol type, k, and for vertical layer, n.  $I_{aer354}$  and  $I_{aer388}$  are radiances  
287 for the 354 and 388 nm channels, respectively.  $K_{354,nk}$  and  $K_{388,nk}$  are the corresponding radiance  
288 Jacobians at 354 and 388 nm, respectively. AI Jacobians can then be calculated by analytic  
289 differentiation of the basic formula in Equation (1), and, after some algebra, we find the following  
290 result:

$$291 \frac{\partial AI}{\partial M_{nk}} = \mathcal{A}_1 K_{354,nk}(\rho_{354}) + \mathcal{A}_2 K_{388,nk}(\rho_{388}) \quad . \quad (6)$$

292 Here,  $\mathcal{A}_1$  and  $\mathcal{A}_2$  are given respectively by Equations (7) and (8), as

$$293 \mathcal{A}_1 = \left( -\frac{100}{I_{aer354}(\rho_{354}) \times \ln 10} \right) \quad , \text{ and} \quad (7)$$

$$294 \mathcal{A}_2 = \left( -\frac{100}{I_{ray354}(R_{388}) \times \ln 10} \right) \frac{\partial I_{ray354}(R_{388})}{\partial R} \left[ \frac{(1 - S_{388} R_{388})^2}{T_{388}} \right] \quad . \quad (8)$$

295 Based on these equations, radiance Jacobians with respect to aerosol particles,  $K_{354,nk}$  and  $K_{388,nk}$ ,  
296 are computed at 354 and 388 nm, respectively, using OMI-reported surface albedo values ( $\rho_{354}$   
297 and  $\rho_{388}$ ), followed by a calculation of the albedo Jacobian  $\frac{\partial I_{aer354}(R_{388})}{\partial R}$  at 354 nm.



298 To check this analytic Jacobian calculation in Eqns. (6)-(8), we compute the aerosol AI  
299 Jacobians using a finite difference (FD) method. Here, the derivative of AI as a function of aerosol  
300 concentration of a species,  $k$ , in layer  $n$ , is computed using

301 
$$\frac{\partial AI}{\partial M_{nk}} = \frac{(AI - AI')}{(C_{nk} - C'_{nk})} . \quad (9)$$

302 Here  $C_{nk}$  and  $C'_{nk}$  are the baseline and perturbed aerosol concentrations, respectively, and AI and  
303 AI' are computed using  $C_{nk}$  and  $C'_{nk}$ , respectively.

304 Figure 2b shows the comparison of Jacobians of dust aerosols estimated from the analytic  
305 and the FD solutions. Dust, smoke, ABF and sea salt aerosol concentrations as a function of  
306 altitude are shown in Figure 2a. To compute FD Jacobians with respect to dust aerosols, a 10%  
307 perturbation is introduced in the dust profiles. A very close match is found between analytic and  
308 FD Jacobians. This validates the analytical solution used in the study. The analytic solution is of  
309 course much faster, as a single call to VLIDORT will deliver all necessary Jacobians at one  
310 wavelength, as compared to 97 separate calls to VLIDORT with the FD calculation (baseline; 4  
311 species perturbations in the 24-layer atmosphere).

312

### 313 3.2 The variational OMI AI assimilation system

314 The OMI AI assimilation system is based on AI simulations (with Jacobians) from the  
315 forward model. Two principles underlay the assimilation procedure. First, we assume that OMI AI  
316 is sensitive to UV-absorbing aerosol particles, such as NAAPS smoke and dust, or that only smoke  
317 and dust are injected high enough into the troposphere to impact AI. Therefore, innovations are  
318 limited to modifications of dust and smoke aerosol properties. For classes that do not strongly  
319 project onto AI, such as sea salt and ABF aerosols, aerosol concentrations are not modified during  
320 the process. Second, contributions of smoke/dust aerosols to AI ( $AI_{\text{smoke}} / AI_{\text{dust}}$ ) prior to



321 assimilation are estimated by multiplying smoke/dust aerosol concentrations from NAAPS with  
322 Jacobians of AI respective of smoke/dust aerosols. The ratio of AI innovation from smoke aerosols  
323 ( $\Delta\text{AI}_{\text{smoke}}$ ) to total AI innovation ( $\Delta\text{AI}$  or OMI AI -  $\text{AI}_{\text{naaps}}$ ) is assumed to be the ratio of  $\text{AI}_{\text{smoke}}$  to  
324  $\text{AI}_{\text{smoke}} + \text{AI}_{\text{dust}}$ . The same assumption holds for dust aerosols.

325 Given these two principles, the overall design concept for the OMI AI assimilation can be  
326 expressed as

327

328  $\mathcal{C}^a = \mathcal{C}^b +$

$$329 \frac{P_{dust} \mathbf{H}_{dust}^T}{\mathbf{H}_{dust}^T P_{dust} \mathbf{H}_{dust} + R} [\mathbf{y} - \mathbf{H}(\mathcal{C}^b)] \times \frac{\mathbf{H}_{dust} \mathbf{C}_{dust}^b}{\mathbf{H}_{dust} \mathbf{C}_{dust}^b + \mathbf{H}_{smk} \mathbf{C}_{smk}^b} + \\ 330 \frac{P_{smk} \mathbf{H}_{smk}^T}{\mathbf{H}_{smk}^T P_{smk} \mathbf{H}_{smk} + R} [\mathbf{y} - \mathbf{H}(\mathcal{C}^b)] \times \frac{\mathbf{H}_{smk} \mathbf{C}_{smk}^b}{\mathbf{H}_{dust} \mathbf{C}_{dust}^b + \mathbf{H}_{smk} \mathbf{C}_{smk}^b}, \quad (10)$$

331

332 where  $\mathcal{C}^b$  and  $\mathcal{C}^a$  are NAAPS aerosol concentrations for the analysis and background fields,  
333 respectively,  $\mathbf{C}_{dust}^b$  and  $\mathbf{C}_{smk}^b$  are background NAAPS particle mass concentrations for dust and  
334 smoke,  $\mathbf{H}(\mathbf{C})$  is the NAAPS forward model that links NAAPS particle mass concentrations to AI,  
335 and  $\mathbf{H}$  is defined as  $\partial\mathbf{H}(\mathbf{C})/\partial\mathbf{C}$ , which is the Jacobian matrix of AI with respect to aerosol  
336 concentrations.  $\mathbf{Y}$  is the observed OMI AI, and  $\mathbf{Y} - \mathbf{H}(\mathcal{C}^b)$  is the innovation of AI, representing the  
337 difference between observed and modeled AI values.

338 The  $\frac{\mathbf{H}_{dust} \mathbf{C}_{dust}^b}{\mathbf{H}_{dust} \mathbf{C}_{dust}^b + \mathbf{H}_{smk} \mathbf{C}_{smk}^b}$  and  $\frac{\mathbf{H}_{smk} \mathbf{C}_{smk}^b}{\mathbf{H}_{dust} \mathbf{C}_{dust}^b + \mathbf{H}_{smk} \mathbf{C}_{smk}^b}$  terms are the fractional contribution  
339 of innovation from dust and smoke aerosol, respectively. These terms are estimated using NAAPS  
340 aerosol concentrations for relatively high aerosol loading cases ( $\text{AOD} > 0.15$ ). For low aerosol  
341 loading ( $\text{AOD} < 0.15$ ) as reported from NAAPS, it is possible that NAAPS could underestimate  
342 aerosol concentrations. Thus, the fractional contribution of innovations is assigned to 1 for the



343 dominant aerosol type based on a NAAPS aerosol climatology (Zhang et al., 2008). Note that the

344 term  $[y - H(C^b)] \times \frac{H_{dust} C_{dust}^b}{H_{dust} C_{dust}^b + H_{smk} C_{smk}^b}$  is in observational space.  $P_{dust}$  and  $P_{smk}$  are model error

345 spatial covariance matrices for dust and smoke (model space) aerosols (e.g. Zhang et al., 2008;

346 2011; 2014).  $R$  is the observation-based error covariance in model space. The

347  $\frac{P_{dust} H_{dust}^T}{H_{dust}^T P_{dust} H_{dust} + R} [y - H(C^b)] \times \frac{H_{dust} C_{dust}^b}{H_{dust} C_{dust}^b + H_{smk} C_{smk}^b}$  and  $\frac{P_{smk} H_{smk}^T}{H_{smk}^T P_{smk} H_{smk} + R} [y - H(C^b)] \times$

348  $\frac{H_{smk} C_{smk}^b}{H_{dust} C_{dust}^b + H_{smk} C_{smk}^b}$  terms represent the estimated increments in model space.

349 The background error covariance matrix is constructed from modeled error variances and

350 error correlations, following the methodology in previous studies (Zhang et al., 2008; 2011). The

351 horizontal background error covariance is generated using the second-order regressive function

352 (SOAR), as shown in Equation 11 (Zhang et al., 2008), or

$$353 C(x, y) = (1 + R_{xy}/L) \exp\left(-\frac{R_{xy}}{L}\right) . \quad (11)$$

354 Here,  $x$  and  $y$  are two given locations, and  $R_{xy}$  is the great circle distance.  $L$  is the averaged error

355 correlation length and is set to 200 km based on Zhang et al. (2008). Similarly, the vertical error

356 correlation between two pressure levels  $p_1$  and  $p_2$  is also based on the SOAR function, this time in

357 pressure space, based on Zhang et al., 2011, is

$$358 C(p_1, p_2) = [1 + \left| \int_{p_1}^{p_2} \frac{d \ln p}{L} \right|] e^{-\left| \int_{p_1}^{p_2} \frac{d \ln p}{L} \right|} . \quad (12)$$

359 Here,  $L$  is a unit-less number representing vertical correlation length and is set to 0.015.

360 The horizontal error variance is based on the RMS error of aerosol concentrations, which

361 is arbitrarily set to  $100 \mu\text{g}/\text{m}^3$  for near-surface dust aerosols (ground to 700 hPa). The RMS error

362 of dust aerosol mass is assumed to decrease as altitude increases, and is set to 50%, 25%, and 1%

363 of the near-surface values for 500-700, 350-500 and 70-350 hPa respectively. Note that different



364 aerosol species have different mass extinction values. Here we assume the modeled error in  
365 aerosol extinction is the same for different aerosol species and thus, the RMS error of smoke  
366 aerosol concentration is scaled by mass extinction cross section ratio between smoke and dust  
367 aerosols. The observational errors are assumed to be non-correlated in this study (e.g. Zhang et  
368 al., 2008). OMI AI values over cloud-free and cloudy skies are used in the study and therefore,  
369 RMS errors of AI are required for both these situations. Note, as suggested by Yu et al. (2012),  
370 for the same above cloud CALIOP AOD, variations in AI are found to be of the order of 1 for  
371 cloud optical depth changing from 2 to 20. Thus, we assume the RMS error of OMI AI is 0.5 for  
372 cloud-free skies, increasing linearly with cloud fraction up to a value of 1 for the 100% overcast.

373 Lastly, we assume that detectable UV absorbing aerosols have AI values larger than 0.8  
374 (e.g. Torres et al., 2013). Therefore, for regions with OMI AI values larger than 0.8, UV absorbing  
375 aerosol particles can both be added or removed from air columns based on innovations, which are  
376 the differences between OMI reported and simulated AI values. For regions with OMI AI values  
377 less than 0.8, innovations are only used to remove UV absorbing aerosol particles from air  
378 columns.

379

380 **4.0 System evaluation & discussion**

381 **4.1 Evaluating the performance of the AI assimilation system over Africa**

382 Using two months of OMI data (July-August, 2007), the performance of OMI AI  
383 assimilation was evaluated around the Africa region (20°S-40°N; 10°W-60°E). The study region  
384 was chosen to examine the performance of OMI AI data assimilation over bright surfaces such as  
385 the deserts of North Africa, as well as study aerosol advection over clouds, in this case smoke off  
386 the west coast of Southern Africa. In this demonstration, two NAAPS runs were performed for



387 the period of July 1 to August 31, 2007, one with and one without the use of OMI AI assimilation  
388 (AI-DA run). Both runs were initialized with the use of NAAPS reanalysis data at 0000 UTC 1  
389 July and do not include any other form of aerosol assimilation.

390 Figure 3a shows the true color composite from Aqua MODIS for July 28, 2007 over the  
391 study region that is obtained from the NASA world view site  
392 (<https://worldview.earthdata.nasa.gov/>; last accessed June 2020). Visible in the image are the dust  
393 plumes from North Africa transported to the Atlantic Ocean, and smoke plumes from Central and  
394 Southern Africa transported to the west coast of South Africa. As indicated by the aggregated  
395 OMI AI data for 1200 UTC 28 July 2007 (Figure 3b), dust plumes from North Africa are  
396 transported to the North corner of the west coast of North Africa. Smoke plumes are also visible  
397 in the OMI AI plot in Southern Africa and are transported to the west coast and over the Atlantic.  
398 Comparing Figure 3a and Figure 3b, smoke plumes, as identified from OMI, are also found over  
399 cloudy regions as indicated from the MODIS visible imagery. Note that Figure 3b shows the OMI  
400 AI data used in the assimilation process and again, AI retrievals over both cloud free and cloudy  
401 conditions are included as suggested by Figure 3b.

402 Figure 3c is the 1200 UTC 28 July 2007 NAAPS AOD product from the natural run. In  
403 comparison, Figure 3d shows the same situation, this time with the use of OMI AI data  
404 assimilation. Comparing 3b with 3d, dust and smoke aerosol patterns as shown from OMI AI  
405 resemble more closely the NAAPS AOD fields after AI assimilation. Over the northeast coast of  
406 Africa, heavy aerosol plumes, as hinted at in NAAPS AOD from the natural run, cover larger  
407 spatial areas than those inferred from OMI AI data. In comparison, NAAPS AOD patterns from  
408 the OMI AI data assimilation cycle closely resemble aerosol patterns as suggested from OMI AI  
409 data. Also shown in Figures 3e and 3f are the simulated AI using NAAPS data from the natural



410 and OMI AI DA runs (data from Figures 3c and 3d) respectively. Clearly, with the use of NAAPS  
411 data from the natural run, simulated OMI AI are overestimated in comparison with OMI AI data  
412 (Figure 3b). Simulated AI patterns with the used of NAAPS data from the OMI AI DA run rather  
413 closely resemble AI patterns from the OMI data, again, indicating the OMI AI DA system is  
414 functioning reasonably as designed.

415 The performance of AI-DA is also evaluated using OMI AI for the whole study period, as  
416 shown in Figure 4. These data are constructed using collocated OMI AI and NAAPS data  
417 according to the conditions introduced in Sec. 3. Here, Figures 4a and 4e are spatial distributions  
418 of two-monthly averaged (July and August 2007) AODs for NAAPS AI-DA and natural runs,  
419 respectively. Figure 4b is the spatial distribution of the simulated AI using NAAPS data from AI-  
420 DA runs, and Figure 4c is the spatial distribution of OMI AI for the two-month period. Figures 4f  
421 and 4g show similar plots to those in Figures 4c and 4d, but this time for NAAPS natural runs.  
422 While simulated AI values from NAAPS natural runs (Figure 4f) are overestimated compared to  
423 OMI AI values (Figure 4g) for the study region, the patterns of simulated AI from NAAPS AI-DA  
424 runs (Figure 4b) are similar to patterns shown from OMI AI (Figure 4c). This is also seen from  
425 Figure 4d, which is the difference between simulated AI from NAAPS AI-DA runs and OMI AI.  
426 In contrast with the situation in Figure 4d, Figure 4h, which is the difference between simulated  
427 AI from NAAPS natural runs and OMI AI, shows much larger differences in AI values.

428 While it is not too difficult to make the model mimic the AI product, proof of real skill lies  
429 in any improvements to AOD calculations. To this end, the performance of OMI AI assimilation  
430 was evaluated with the use of AERONET data. Figure 5a shows the inter-comparison of NAAPS  
431 AOD versus AERONET AOD at 0.55  $\mu\text{m}$ . A total of 1450 collocated pairs of NAAPS and  
432 AERONET data were compiled for the study region over the two months test period. Comparing



433 with AERONET data, NAAPS AOD from the natural run had a correlation of 0.64, a mean  
434 absolute error in AOD of 0.17, and an RMSE of 0.25. In comparison, with AI assimilation,  
435 NAAPS AOD correlations to AERONET increased to 0.72 (Figure 5b), the absolute error reduced  
436 to 0.12, and RMSE reduced to 0.18, both roughly a 30% reduction. Note that AERONET AOD  
437 values are only available for lines-of-sight that are free of cloud presence for the sun photometer  
438 instruments. Also, the slope of AERONET versus NAAPS AOD is 0.93 for the NAAPS natural  
439 runs, and a similar slope of 0.92 is found for the NAAPS AI-DA runs.

440

#### 441 **4.2 Inter-comparison with AOD data assimilation**

442 Typically, NAAPS reanalyses are constructed through assimilation of MISR and MODIS  
443 aerosol products (NAAPS AOD assimilation). Thus, the performances of NAAPS AOD and AI-  
444 DA assimilations are compared against AERONET data. Figure 5c shows the comparison of  
445 AERONET AOD and NAAPS AOD after AOD assimilation, while Figure 5b shows a similar plot  
446 but using NAAPS data from AI-DA. A better correlation between AERONET and NAAPS data  
447 of 0.82 and a slope of 1.01 are found using AOD data assimilation. In comparison, the correlation  
448 is 0.72 and the slope is 0.92 for the AI-DA runs. Slightly better RMSE (0.15 versus 0.18) and  
449 absolute error (0.11 versus 0.12) values are also found for the AOD data assimilation runs. This  
450 result is not surprising as OMI AI provides only a proxy for aerosol properties while passive-based  
451 AOD retrievals are often considered as a more reliable parameter for representing column-  
452 integrated aerosol properties. But still, the evaluation efforts are over cloud-free line-of-sight as  
453 detected from AERONET, AI DA may further assist traditional AOD data assimilation by proving  
454 AI assimilation over cloudy regions.

455

#### 456 **4.3 Sensitivity test**



457 As mentioned in Section 3, aerosol properties for non-smoke aerosol types were obtained  
458 from the NASA GEOS-5 model (e.g. Colarco et al., 2014; Buchard et al., 2015). Yet, different  
459 smoke aerosol SSA values are used in this study, as values for central Africa have a strong seasonal  
460 dependency (e.g. Eck et al., 2013). While SSA values of 0.85 and 0.86 are used for the 354 and  
461 388 nm channels, respectively, in our study, we have also examined the sensitivity of simulated  
462 OMI AI with respect to differing SSA values (Figure 6). Figures 6a-c show the simulated AI at  
463 1200 UTC 28 July 2007 using NAAPS reanalysis data (Lynch et al, 2016) for three scenarios: SSA  
464 values at 354 and 388 nm of 0.84 and 0.84 (Figure 6a), 0.85 and 0.85 (Figure 6b) and 0.86 and  
465 0.86 (Figure 6c). Over the central Africa area, where smoke plumes are expected, simulated OMI  
466 AI patterns are similar for Figures 6a and 6b, but reduced values in AI are found when using higher  
467 SSA values of 0.86 at both 354 and 388 nm. This is further confirmed by the averaged AI for the  
468 smoke region over central Africa (-0.5° to -15.5° latitude and 10.5° to 30.5° E longitude; indicated  
469 using the black box in Figure 6f) of 0.96, 0.94 and 0.78 for Figures 6a, 6b and 6c respectively.

470 Figures 6d-f show the sensitivity for adjustments of the SSA values at 388nm while  
471 maintaining a fixed SSA value of 0.85 at 354 nm. Here the SSA values at 388 nm are set to 0.85,  
472 0.855 and 0.86 for Figures 6d, 6e and 6f respectively. Interestingly, the spectral dependence of  
473 SSA seems to affect the simulated AI significantly, and this phenomenon has also been reported  
474 by previous studies (e.g. Hammer et al., 2017). The averaged AI values over central Africa (again,  
475 indicated by the black box in Figure 6f) are 0.94, 1.11 and 1.32 for 388 nm SSAs of 0.85, 0.855  
476 and 0.86, respectively. This exercise suggests that simulated AI is a strong function of SSA, so  
477 that both the spectral dependence of SSA values at 354 and 388 nm and reliable SSA values are  
478 needed on a regional basis for future applications.



479         Interestingly, although simulated AI values are significantly affected by perturbing SSA  
480         values as shown in Figure 6, less significant impacts are observed for NAAPS AOD. This is found  
481         by running the OMI AI DA for 1200UTC, July 28, 2015 for SSA values used in generating Figure  
482         6. For example, for the black box highlighted region in Figure 6f, the averaged values for the  
483         simulated OMI AI are 0.96, 0.94 and 0.78 for using SSA values at 354 / 388 nm channels of 0.84  
484         / 0.84, 0.85 / 0.85 and 0.86 / 0.86, respectively. The corresponding NAAPS AODs are found to  
485         be 0.559, 0.560 and 0.585 after OMI AI DA, which is a change of less than 5%. Similar, by fixing  
486         the SSA value of the 354 nm channel as 0.85 and perturbing SSA values at 388 nm from 0.85 to  
487         0.86, a ~30% change is found in simulated OMI AI (from 0.94 to 1.32), yet a ~10% change is  
488         found for the NAAPS AOD (from 0.560 to 0.504) after OMI AI DA.

489         It is also of interest to investigate the changes in aerosol vertical distributions due to the  
490         OMI AI DA. For this exercise, we selected the 1200 UTC 28 July 2007 case and compared vertical  
491         distributions of smoke and dust aerosols near the peak AI value of the smoke plume (9.5°S and  
492         20.5°E) for the NAAPS natural and AI DA runs (Figure 7a). As shown in Figure 7a, the  
493         corrections to dust and smoke aerosol concentrations from the AI DA system seem to be systematic  
494         changes across the majority of vertical layers, instead of moving dust or smoke aerosol plumes  
495         vertically. As dust aerosol concentrations are reduced at all layers and a systematic correction to  
496         smoke aerosol concentrations, although non-linear, is also observed. AI assimilation helps reduce  
497         the amount of upper troposphere dust (likely to be artifact) but does change the layer centroid  
498         slightly upwards. We have also evaluated NAAPS vertical distributions near a peak dust plume  
499         region (25.5°N and 12.5°W) for the 12Z 28 July 2007 case as shown in Figure 7b. Similar to  
500         Figure 7a, a non-linear correction to dust aerosol concentrations is also observed across the vertical  
501         domain.



502

503 **4.4 Issues and discussions**

504 The OMI AI data assimilation system is a proxy for all-sky, all-band modeling system  
505 radiance assimilation. It contains all the necessary components for such radiance assimilation,  
506 including a forward model for simulating radiances and AI values and their Jacobians, based on a  
507 full vector linearized radiative transfer model called for every observation. Therefore, the  
508 computational burden is a direct issue associated with the deployment of calls to a radiative transfer  
509 model for each observation. For the study area in this work, after binning OMI AI data into a  
510  $1^\circ \times 1^\circ$  (Latitude/Longitude) product, it still takes about  $\sim 1$  CPU day for NAAPS to run for one  
511 month of model time. Clearly, there will be an unavoidable computational burden of some sort  
512 for OMI AI assimilation and by extension, for future radiance assimilation in the UV/visible  
513 spectrum for aerosol analyses. Performance enhancement methods, such as parallel processing  
514 (the VLIDORT software is thread-safe and can be used in parallel environments such as OpenMP),  
515 or fast look-up-table extraction based on neural-networks and trained data sets of forward  
516 simulation, must be explored in order to enable such assimilation applications in near real time on  
517 a global scale.

518 In contrast with the assimilation of retrieved aerosol properties, both aerosol absorption  
519 and scattering need to be accounted for when assimilating radiance or OMI AI in the UV spectrum.  
520 This requires the inclusion of more dynamic aerosol optical properties into the data assimilation  
521 process, and properties that vary with region and season. As noted already, even for biomass  
522 burning aerosols over South Africa, lower single scattering albedo values were found at earlier  
523 stages of burning seasons (e.g. Eck et al., 2013). A look-up-table of aerosol optical properties as



524 functions of region and season will be needed for global implications of OMI AI as well as future  
525 radiance assimilation for aerosol modeling.

526 OMI AI is sensitive to above-cloud UV-absorbing aerosols (e.g. Yu et al., 2012; Alfaro-  
527 Contreras et al., 2014), and therefore, OMI AI values over cloudy scenes were also used in this  
528 study. However, OMI AI cannot be used to infer aerosol properties for aerosol plumes beneath a  
529 cloud deck. For regions with high clouds, the use of OMI AI data assimilation will likely result in  
530 an underestimation of AOD as below-cloud aerosol plumes are not accounted for. Therefore, only  
531 OMI AI data over low cloud scenes are to be used for aerosol assimilation efforts. In addition,  
532 although some quality assurance steps were applied in this study for the OMI AI data, lower AI  
533 values were observed over glint regions near the west coast of Africa. Abnormally high OMI AI  
534 values are also seen near the Arctic region - this may be related to the presence of floating ice  
535 sheets. Thus, innovative and detailed data screening and quality assurance steps are needed to  
536 exclude potentially noisy OMI AI retrievals and for further application of OMI AI data  
537 assimilation on a global scale.

538 Even with these known issues, OMI AI assimilation as presented in the study illustrates a  
539 new method for assimilating non-conventional aerosol products. Bearing in mind that OMI AI  
540 assimilation is essentially radiance assimilation in the UV spectrum, this study demonstrates the  
541 potential of directly assimilating satellite radiance in the UV/visible spectrum for aerosol modeling  
542 and analyses.

543

## 544 **5.0 Conclusions**

545 The OMI aerosol index (AI), which measures the differences between simulated radiances  
546 over Rayleigh sky and observed radiances at 354 nm, has been used to detect the presence of  
547 absorbing aerosols over both dark and bright surfaces. We have constructed a new assimilation



548 system, based on the VLIDORT radiative transfer code as the major component of the forward  
549 model, for the direct assimilation of OMI AI. The aim is to improve accuracies of aerosol analyses  
550 over bright surfaces such as cloudy regions and deserts.

551 The performance of the OMI AI data assimilation system was evaluated over South-Central  
552 and Northern Africa regions for the period of 01 July -31 August 2007. This evaluation was done  
553 through inter-comparing NAAPS analyses with and without the inclusion of OMI AI data  
554 assimilation. Besides cloud-free AI retrievals over dark surfaces, OMI AI retrievals over desert  
555 regions and over areas were also considered. When compared against AERONET data, a total of  
556 ~28% reduction in Root-Mean-Square-Error (RMSE) with a ~32% reduction in absolute error  
557 were found for NAAPS analyses with the use of OMI AI assimilation. Also, NAAPS analyses  
558 with the inclusion of OMI AI data assimilation show similar aerosol patterns to those in the OMI  
559 AI data sets, showing that our OMI AI data assimilation system works as expected.

560 This study also suggests that NAAPS analyses with OMI AI data assimilation cannot out-  
561 perform NAAPS reanalyses data that were incorporated with MODIS and MISR AOD  
562 assimilation, and validated against AERONET data. This is not surprising, as OMI AI is only a  
563 proxy for the AOD and is sensitive to other factors such as surface albedo and aerosol vertical  
564 distribution. Also, AERONET data are only available over cloud-free field of views, so the  
565 performance of our OMI AI data assimilation system over cloudy regions has not been evaluated.

566 There are a number of issues arising from our study. For example, aerosol optical  
567 properties are needed for the OMI AI-DA system - these have strong regional and temporal  
568 signatures that need to be carefully quantified before applying them to the AI-DA on a global scale.  
569 Also, OMI AI retrievals are rather noisy and contain known and unknown biases. Abnormally  
570 high OMI AI values are found over mountain regions as well the polar regions. Sporadic high AI



571 values are also known to occur, for reasons that are still not properly understood. Even though  
572 quality assurance steps were proposed in this study, detailed analysis of OMI AI data are needed  
573 for future implementation of OMI AI data assimilation for aerosol studies.

574 Lastly, AI values are derived from radiances and thus, the AI-DA system presented in the  
575 study can be thought of as a radiance assimilation system for the UV spectrum. This is because  
576 the AI-DA system contains all necessary components for radiance assimilation, based on a forward  
577 model for calculating not only simulated satellite radiances, but also the aerosol-profile Jacobians  
578 of these radiance, both quantities as functions of observation conditions. This study is among the  
579 first attempts at radiance assimilation at the UV spectrum and indicates the future potential for  
580 direct radiance assimilation at the UV and visible spectra for aerosol analyses and forecasts.

581

582 **Author contributions.** All authors contributed to the overall design of the study. Authors JZ and  
583 RS coded the system. Author JSR provided valuable suggestions though the study. Author PX  
584 assist with the evaluation of the system.

585

586 **Code and data availability:** The VLIDORT radiative transfer model is available to the public  
587 through contacting RT solutions Inc. ([http://www.rtslidort.com/mainprod\\_vlidort.html](http://www.rtslidort.com/mainprod_vlidort.html)). The  
588 NAAPS model belongs to the Naval Research Laboratory and is not publically available. The  
589 NAAPS reanalysis data are available from the USGODAE web site  
590 ([https://nrlgodaе1.nrlmry.navy.mil/cgi-bin/datalist.pl?dset=nrl\\_naaps\\_reanalysis&summary=Go](https://nrlgodaе1.nrlmry.navy.mil/cgi-bin/datalist.pl?dset=nrl_naaps_reanalysis&summary=Go)).  
591 The OMI OMAERUV data are available from the NASA's Goddard Earth Sciences Data and  
592 Information Services Center (GES) DISC;



593    [https://disc.gsfc.nasa.gov/datasets/OMAERUV\\_003/summary](https://disc.gsfc.nasa.gov/datasets/OMAERUV_003/summary)). AERONET data are obtained  
594    from the NASA AERONET webpage (<https://aeronet.gsfc.nasa.gov/>).).

595

596    **Competing interests.** The authors claim no competing interests.

597

598    **Acknowledgements.** We thank the NASA AERONET group for the sun-photometer data used in  
599    the study. “We acknowledge the use of imagery from the NASA Worldview application  
600    (<https://worldview.earthdata.nasa.gov>), part of the NASA Earth Observing System Data and  
601    Information System (EOSDIS).”

602

603    **Financial support.** This study is supported by the NASA grant NNX17AG52G. Co-Author JSR  
604    was supported by the Office of Naval Research Code 322.

605

606  
607



608 **References:**

609 Alfaro-Contreras, R., Zhang, J., Campbell, J. R., and Reid, J. S.: Investigating the frequency and  
610 trends in global above-cloud aerosol characteristics with CALIOP and OMI, *Atmos. Chem.*  
611 *Phys.*, 16, 47-69, doi:10.5194/acp-16-47-2016, 2016.

612 Alfaro-Contreras R., Zhang, J., Campbell, J. R., Holz, R. E., and Reid, J. S.: Evaluating the Impact  
613 of Aerosol Particles above Cloud on Cloud Optical Depth Retrievals from MODIS, *J.*  
614 *Geophys. Res. Atmos.*, 119, 5410–5423, doi:10.1002/2013JD021270, 2014.

615 Benedetti, A., et al., Aerosol analysis and forecast in the European Centre for Medium-Range  
616 Weather Forecasts Integrated Forecast System: 2. Data assimilation, *J. Geophys. Res.*, 114,  
617 D13205, doi:10.1029/2008JD011115, 2009.

618 Bessho, K., Date, K., Hayashi, M., Ikeda, A., Imai, T., Inoue, H., Kumagai, Y., Miyakawa, T.,  
619 Murata, H., Ohno, T., Okuyama, A., Oyama, R., Sasaki, Y., Shimazu, Y., Shimoji, K.,  
620 Sumida, Y., Suzuki, M., Taniguchi, H., Tsuchiyama, H., Uesawa, D., Yokota, H., &  
621 Yoshida, R.: An Introduction to Himawari-8/9- Japan's New-Generation Geostationary  
622 Meteorological Satellites. *Journal of the Meteorological Society of Japan. Ser. II*, 94(2),  
623 151–183. <https://doi.org/10.2151/jmsj.2016-009>, 2016.

624 Buchard, V., Randles, C., Silva, A., Darmenov, A., Colarco, P., Govindaraju, R., Ferrare, R., Hair,  
625 J., Beyersdorf, A., Ziembba, L., Yu, H.: The MERRA-2 Aerosol Reanalysis, 1980 Onward.  
626 Part II: Evaluation and Case Studies *Journal of Climate* <https://dx.doi.org/10.1175/jcli-d-16-0613.1>, 2017.

628 Buchard, V., da Silva, A. M., Colarco, P. R., Darmenov, A., Randles, C. A., Govindaraju, R.,  
629 Torres, O., Campbell, J., and Spurr, R.: Using the OMI aerosol index and absorption



630 aerosol optical depth to evaluate the NASA MERRA Aerosol Reanalysis, *Atmos. Chem.*  
631 *Phys.*, 15, 5743–5760, <https://doi.org/10.5194/acp-15-5743-2015>, 2015.

632 Cochrane, S. P., Schmidt, K. S., Chen, H., Pilewskie, P., Kittelman, S., Redemann, J., LeBlanc,  
633 S., Pistone, K., Kacenelenbogen, M., Segal Rozenhaimer, M., Shinozuka, Y., Flynn, C.,  
634 Platnick, S., Meyer, K., Ferrare, R., Burton, S., Hostetler, C., Howell, S., Freitag, S.,  
635 Dobrucki, A., and Doherty, S.: Above-cloud aerosol radiative effects based on ORACLES  
636 2016 and ORACLES 2017 aircraft experiments, *Atmos. Meas. Tech.*, 12, 6505–6528,  
637 <https://doi.org/10.5194/amt-12-6505-2019>, 2019.

638 Colarco, P. R., Nowottnick, E. P., Randles, C. A., Yi, B., Yang, P., Kim, K.-M., Smith, J. A. and  
639 Bardeen, C. G.: Impact of radiatively interactive dust aerosols in the NASA GEOS-5  
640 climate model: sensitivity to dust particle shape and refractive index. *Journal of*  
641 *Geophysical Research: Atmospheres*, 119(2), 753–786.  
642 <https://doi.org/10.1002/2013JD020046>, 2014.

643 Dai, A.: Precipitation characteristics in eighteen coupled climate models. *Journal of Climate*, 19,  
644 4605–4630, 2006.

645 Eck, T. F., Holben, B. N., Reid, J. S., Mukelabai, M. M., Piketh, S. J., Torres, O., Jethva, H. T.,  
646 Hyer, E. J., Ward, D. E., Dubovik, O., and Sinyuk, A.: A seasonal trend of single scattering  
647 albedo in southern African biomass-burning particles: Implications for satellite products  
648 and estimates of emissions for the world's largest biomass-burning source, *J. Geophys.*  
649 *Res.-Atmos.*, 118, 6414–6432, 2013.

650 Giles, D. M., Sinyuk, A., Sorokin, M. G., Schafer, J. S., Smirnov, A., Slutsker, I., Eck, T. F.,  
651 Holben, B. N., Lewis, J. R., Campbell, J. R., Welton, E. J., Korkin, S. V., and Lyapustin,  
652 A. I.: Advancements in the Aerosol Robotic Network (AERONET) Version 3 database –



653 automated near-real-time quality control algorithm with improved cloud screening for Sun  
654 photometer aerosol optical depth (AOD) measurements, *Atmos. Meas. Tech.*, 12, 169–209,  
655 <https://doi.org/10.5194/amt-12-169-2019>, 2019.

656 Hammer, M. S., Martin, R. V., van Donkelaar, A., Buchard, V., Torres, O., Ridley, D. A., and  
657 Spurr, R. J. D.: Interpreting the ultraviolet aerosol index observed with the OMI satellite  
658 instrument to understand absorption by organic aerosols: implications for atmospheric  
659 oxidation and direct radiative effects, *Atmos. Chem. Phys.*, 16, 2507–2523,  
660 <https://doi.org/10.5194/acp-16-2507-2016>, 2016.

661 Herman, J. R., Bhartia, P. K., Torres, O., Hsu, C., Seftor, C., and Celarier, E.: Global distribution  
662 of UV-absorbing aerosols from Nimbus 7/TOMS data, *J. Geophys. Res.*, 102(D14),  
663 16911–16922, doi:[10.1029/96JD03680](https://doi.org/10.1029/96JD03680)., 1997.

664 Holben, B. N., and coauthors: AERONET—A Federated Instrument Network and Data Archive  
665 for Aerosol Characterization. *Remote Sensing of Environment*, 66(1), 1–16.  
666 [https://doi.org/10.1016/S0034-4257\(98\)00031-5](https://doi.org/10.1016/S0034-4257(98)00031-5), 1998.

667 Hogan, T.F., Liu, M., Ridout, J. A., Peng, M. S., Whitcomb, T. R., Ruston, B. C., Reynolds, C. A.,  
668 Eckermann, S. D., Moskaitis, J. R., Baker, N. L., McCormack, J. P., Viner, K. C., McLay,  
669 J. G., Flatau, M. K., Xu, L., Chen, C., and Chang, S. W.: The Navy Global Environmental  
670 Model, *Oceanography*, 27(3):116–125, <https://doi.org/10.5670/oceanog.2014.73.>, 2014.

671 Hsu, N. C., Lee, J., Sayer, A. M., Kim, W., Bettenhausen, C., and Tsay, S.-C.: VIIRS Deep Blue  
672 aerosol products over land: Extending the EOS long-term aerosol data records, *J. Geophys.*  
673 *Res.-Atmos.*, 124, 4026–4053, <https://doi.org/10.1029/2018JD029688>, 2019.



674 Hsu, N. C., Jeong, M.-J., Bettenhausen, C., Sayer, A. M., Hansell, R., Seftor, C. S., Huang, J., and  
675 Tsay S.-C.: Enhanced Deep Blue aerosol retrieval algorithm: The second generation, *J.  
676 Geophys. Res. Atmos.*, 118, doi:10.1002/jgrd.50712, 2013.

677 Hsu, N. C., Gautam, R., Sayer, A. M., Bettenhausen, C., Li, C., Jeong, M. J., Tsay, S.-C., and  
678 Holben, B. N.: Global and regional trends of aerosol optical depth over land and ocean  
679 using SeaWiFS measurements from 1997 to 2010, *Atmos. Chem. Phys.*, 12, 8037–8053,  
680 https://doi.org/10.5194/acp-12-8037-2012, 2012.

681 Hyer, E. J., Reid, J. S., and Zhang, J.: An over-land aerosol optical depth data set for data  
682 assimilation by filtering, correction, and aggregation of MODIS Collection 5 optical depth  
683 retrievals, *Atmos. Meas. Tech.*, 4, 379–408, doi:10.5194/amt-4-379-2011, 2011.

684 Joyce, J. R., Janowiak, E. J., Arkin, P. A., and Xie, P.: CMORPH: A method that produces global  
685 precipitation estimates from passive microwave and infrared data at high spatial and  
686 temporal resolution, *J. Hydrometeor.*, 5, 487–503, 2004.

687 Kahn, R. A., Gaitley, B. J., Garay, M. J., Diner, D. J., Eck, T. F., Smirnov, A. and Holben B. N.:  
688 Multiangle Imaging SpectroRadiometer global aerosol product assessment by comparison  
689 with the Aerosol Robotic Network, *J. Geophys. Res.*, 115, D23209,  
690 doi:[10.1029/2010JD014601](https://doi.org/10.1029/2010JD014601), 2010.

691 Lee, J., Hsu, N.C., Bettenhausen, C., Sayer, A. M., Seftor, C. J., and Jeong, M.-J.: Retrieving the  
692 height of smoke and dust aerosols by synergistic use of VIIRS, OMPS, and CALIOP  
693 observations, *J. Geophys. Res. Atmos.*, 120, 8372–8388, doi:10.1002/2015JD023567, 2015.

694 Levelt, P. F., Joiner, J., Tamminen, J., Veefkind, J. P., Bhartia, P. K., Stein Zweers, D. C., Duncan,  
695 B. N., Streets, D. G., Eskes, H., van der A, R., McLinden, C., Fioletov, V., Carn, S., de  
696 Laat, J., DeLand, M., Marchenko, S., McPeters, R., Ziemke, J., Fu, D., Liu, X., Pickering,



697 K., Apituley, A., González Abad, G., Arola, A., Boersma, F., Chan Miller, C., Chance, K.,  
698 de Graaf, M., Hakkarainen, J., Hassinen, S., Ialongo, I., Kleipool, Q., Krotkov, N., Li, C.,  
699 Lamsal, L., Newman, P., Nowlan, C., Suleiman, R., Tilstra, L. G., Torres, O., Wang, H.,  
700 and Wargan, K.: The Ozone Monitoring Instrument: overview of 14 years in space, *Atmos.*  
701 *Chem. Phys.*, 18, 5699–5745, <https://doi.org/10.5194/acp-18-5699-2018>, 2018.

702 Levy, R. C., Mattoo, S., Munchak, L. A., Remer, L. A., Sayer, A. M., Patadia, F., and Hsu N. C.:  
703 The Collection 6 MODIS aerosol products over land and ocean, *Atmos. Meas. Tech.*, 6,  
704 2989–3034, doi:10.5194/amt-6-2989-2013, 2013.

705 Li, Z., Zang, Z., Li, Q. B., Chao, Y., Chen, D., Ye, Z., Liu, Y., and Liou, K. N.: A three-dimensional  
706 variational data assimilation system for multiple aerosol species with WRF/Chem and an  
707 application to PM<sub>2.5</sub> prediction, *Atmos. Chem. Phys.*, 13, 4265–4278,  
708 <https://doi.org/10.5194/acp-13-4265-2013>, 2013.

709 Lynch, P., Reid, J. S., Westphal, D. L., Zhang, J., Hogan, T. F., Hyer, E. J., Curtis, C. A., Hegg,  
710 D. A., Shi, Y., Campbell, J. R., Rubin, J. I., Sessions, W. R., Turk, F. J., and Walker, A.  
711 L.: An 11-year global gridded aerosol optical thickness reanalysis (v1.0) for atmospheric  
712 and climate sciences, *Geosci. Model Dev.*, 9, 1489–1522, <https://doi.org/10.5194/gmd-9-1489-2016>, 2016.

713 Pistone, K., Redemann, J., Doherty, S., Zuidema, P., Burton, S., Cairns, B., Cochrane, S., Ferrare,  
714 R., Flynn, C., Freitag, S., Howell, S. G., Kacenelenbogen, M., LeBlanc, S., Liu, X.,  
715 Schmidt, K. S., Sedlacek III, A. J., Segal-Rozenhaimer, M., Shinozuka, Y., Stamnes, S.,  
716 van Diedenhoven, B., Van Harten, G., and Xu, F.: Intercomparison of biomass burning  
717 aerosol optical properties from in situ and remote-sensing instruments in ORACLES-2016,  
718 *Atmos. Chem. Phys.*, 19, 9181–9208, <https://doi.org/10.5194/acp-19-9181-2019>, 2019.



720 Randles, C., Silva, A., Buchard, V., Colarco, P., Darmenov, A., Govindaraju, R., Smirnov, A.,  
721 Holben, B., Ferrare, R., Hair, J., Shinozuka, Y., Flynn, C.: The MERRA-2 Aerosol  
722 Reanalysis, 1980 Onward. Part I: System Description and Data Assimilation Evaluation,  
723 Journal of Climate <https://dx.doi.org/10.1175/jcli-d-16-0609.1>, 2017.

724 Reid, J. S., Hyer, E. J., Prins, E. M., Westphal, D. L., Zhang, J., Wang, J., Christopher, S. A.,  
725 Curtis, C. A., Schmidt, C. C., Eleuterio, D. P., Richardson, K. A., and Hoffman, J. P.:  
726 Global monitoring and forecasting of biomass-burning smoke: Description and lessons  
727 from the Fire Locating and Modeling of Burning Emissions (FLAMBE) program, IEEE J.  
728 Sel. Top. Appl., 2, 144–162, 2009.

729 Rubin J. I., Reid, J. S., Hansen, J. A., Anderson, J. L., Holben, B. N., Lynch, P., Westphal, D. L.,  
730 and Zhang, J.: Assimilation of AERONET and MODIS AOT observations using  
731 Variational and Ensemble Data Assimilation Methods and Its Impact on Aerosol  
732 Forecasting Skill, J. Geophys. Res., DOI: 10.1002/2016JD026067, 2017.

733 Saide, P. E., Carmichael, G. R., Liu, Z., Schwartz, C. S., Lin, H. C., da Silva, A. M., and Hyer, E.:  
734 Aerosol optical depth assimilation for a size-resolved sectional model: impacts of  
735 observationally constrained, multi-wavelength and fine mode retrievals on regional scale  
736 analyses and forecasts, Atmos. Chem. Phys., 13, 10425–10444,  
737 <https://doi.org/10.5194/acp-13-10425-2013>, 2013.

738 Schutgens, N. A. J., Miyoshi, T., Takemura, T., and Nakajima, T.: Applying an ensemble Kalman  
739 filter to the assimilation of AERONET observations in a global aerosol transport model,  
740 Atmos. Chem. Phys., 10, 2561–2576, <https://doi.org/10.5194/acp-10-2561-2010>, 2010.



741 Schwartz, C. S., Liu, Z., Lin, H.-C., and McKeen, S. A.: Simultaneous three-dimensional  
742 variational assimilation of surface fine particulate matter and MODIS aerosol optical depth,  
743 *J. Geophys. Res.*, 117, D13202, doi:10.1029/2011JD017383, 2012.

744 Sekiyama, T. T., Tanaka, T. Y., Shimizu, A., and Miyoshi, T.: Data assimilation of CALIPSO  
745 aerosol observations, *Atmos. Chem. Phys.*, 10, 39–49, <https://doi.org/10.5194/acp-10-39-2010>, 2010.

746 Sessions, W. R., Reid, J. S., Benedetti, A., Colarco, P. R., da Silva, A., Lu, S., Sekiyama, T.,  
747 Tanaka, T. Y., Baldasano, J. M., Basart, S., Brooks, M. E., Eck, T. F., Iredell, M., Hansen,  
748 J. A., Jorba, O. C., Juang, H.-M. H., Lynch, P., Morcrette, J.-J., Moorthi, S., Mulcahy, J.,  
749 Pradhan, Y., Ringer, M., Sampson, C. B., Wang, J., and Westphal, D. L.: Development  
750 towards a global operational aerosol consensus: basic climatological characteristics of the  
751 International Cooperative for Aerosol Prediction Multi-Model Ensemble (ICAP-MME),  
752 *Atmos. Chem. Phys.*, 15, 335–362, <https://doi.org/10.5194/acp-15-335-2015>, 2015.

753 Shi Y., Zhang J., J.S. Reid, B. Liu, E.J. Hyer, Critical evaluation of cloud contamination in the  
754 MISR aerosol products using MODIS cloud masking products, *Atmos. Meas. Tech.*, 7,  
755 1791–1801, doi:10.5194/amt-7-1791-2014, 2014.

756 Spurr, R. J. D., and Christi. M.: The LIDORT and VLIDORT Linearized Scalar and Vector  
757 Discrete Ordinate Radiative Transfer Models: An Update for the last 10 Years, *Light*  
758 *Scattering Reviews*, Volume 12, ed. A. Kokhanovsky, Springer, 2019.

759 Spurr, R. J. D.: VLIDORT: A linearized pseudo-spherical vector discrete ordinate radiative  
760 transfer code for forward model and retrieval studies in multilayer multiple scattering  
761 media, *J. Quant. Spectrosc. Radiat. Transfer*, 102(2), 316–342,  
762 doi:10.1016/j.jqsrt.2006.05.005, 2006.



764 Torres, O., Bhartia, P. K., Jethva, H., and Ahn, C.: Impact of the ozone monitoring instrument row  
765 anomaly on the long-term record of aerosol products, *Atmos. Meas. Tech.*, 11, 2701–2715,  
766 <https://doi.org/10.5194/amt-11-2701-2018>, 2018.

767 Torres, O., Ahn, C., and Chen, Z.: Improvements to the OMI near-UV aerosol algorithm using A-  
768 train CALIOP and AIRS observations, *Atmos. Meas. Tech.*, 6, 3257–3270,  
769 <https://doi.org/10.5194/amt-6-3257-2013>, 2013.

770 Torres, O., Jethva, H., and Bhartia, P. K.: Retrieval of Aerosol Optical Depth above Clouds from  
771 OMI Observations: Sensitivity Analysis and Case Studies. *J. Atmos. Sci.*, 69, 1037–1053,  
772 <https://doi.org/10.1175/JAS-D-11-0130.1>, 2012.

773 Torres, O., Tanskanen, A., Veihelmann, B., Ahn, C., Braak, R., Bhartia, P. K., Veefkind, P., Levelt,  
774 P.: Aerosols and surface UV products from Ozone Monitoring Instrument observations:  
775 An overview. *Journal of Geophysical Research*, 112, D24S47.  
776 <https://doi.org/10.1029/2007JD008809>, 2007.

777 Uno, I., Yumimoto, K., Shimizu, A., Hara, Y., Sugimoto, N., Wang, Z., Liu, Z., and Winker D.  
778 M.: 3D structure of Asian dust transport revealed by CALIPSO lidar and a 4DVAR dust  
779 model, *Geophys. Res. Lett.*, 35, L06803, doi:10.1029/2007GL032329, 2008.

780 Westphal, D. L., Toon, O. B., and Carlson, T. N.: A case study of mobilization and transport of  
781 Saharan dust. *J. Atmos. Sci.*, 45, 2145–2175, 1988.

782 Witek, M. L., Flatau, P. J., Quinn, P. K., Westphal, D. L., Global sea-salt modeling: results and  
783 validation against multicampaign shipboard measurements, *J. Geophys. Res.*, 112, p.  
784 D08215, [10.1029/2006JD007779](https://doi.org/10.1029/2006JD007779), 2007.

785 Xian, P., Reid, J.S., Turk, J.F., Hyer, E.J. and Westphal, D.L.: Impact of modeled versus satellite  
786 measured tropical precipitation on regional smoke optical thickness in an aerosol transport



787 model, Geophysical Research Letters, 36, L16805,  
788 https://doi.org/10.1029/2009GL038823, 2009.

789 Yu, H., Zhang, Y., Chin M., Liu Z., Omar A., Remer L. A., Yang Y., Yuan T. and Zhang J.: An  
790 Integrated Analysis of Aerosol above Clouds from A-Train Multi-sensor Measurements,  
791 Remote Sens. Environ., 121, 125–131, <https://doi.org/10.1016/j.rse.2012.01.011>, 2012.

792 Yumimoto, K., Uno, I., Sugimoto, N., Shimizu, A., Liu, Z., and Winker, D. M.: Adjoint inversion  
793 modeling of Asian dust emission using lidar observations, Atmos. Chem. Phys., 8, 2869–  
794 2884, <https://doi.org/10.5194/acp-8-2869-2008>, 2008.

795 Zhang J., Reid, J. S., Campbell, J. R., Hyer, E. J., and Westphal, D. L.: Evaluating the Impact of  
796 Multi-Sensor Data Assimilation on A Global Aerosol Particle Transport Model. J.  
797 Geophys. Res. Atmos., 119, 4674–4689, doi:[10.1002/2013JD020975](https://doi.org/10.1002/2013JD020975), 2014.

798 Zhang, J., Campbell, J. R., Reid, J. S., Westphal, D. L., Baker, N. L., Campbell, W. F., and Hyer,  
799 E. J.: Evaluating the impact of assimilating CALIOP-derived aerosol extinction profiles on  
800 a global mass transport model, Geophys. Res. Lett., Vo. 38, No. 14, L14801, doi:  
801 10.1029/2011GL04773, 2011.

802 Zhang, J. and Reid, J. S.: A decadal regional and global trend analysis of the aerosol optical depth  
803 using a data-assimilation grade over-water MODIS and Level 2 MISR aerosol products,  
804 Atmos. Chem. Phys. Discuss., 10, 18879-18917, doi:10.5194/acpd-10-18879-2010, 2010.

805 Zhang, J., Reid, J. S., Westphal, D. L., Baker, N. L., and Hyer, E. J.: A system for operational  
806 aerosol optical depth data assimilation over global oceans, J. Geophys. Res., 113, No. D10,  
807 D10208, doi: 10.1029/2007JD009065, 2008.



808 Zhang, J. and Reid., J.S.: MODIS Aerosol Product Analysis for Data Assimilation: Assessment  
809 of Level 2 Aerosol Optical Thickness Retrievals, *J. Geophysical Research-Atmospheres*,  
810 VOL. 111, D22207, doi:10.1029/2005JD006898, 2006.  
811  
812



813 Table 1. Mass extinction cross-sections ( $\sigma$ ,  $\text{m}^2/\text{g}$ ) and single scattering albedos ( $\omega_o$ ) used in  
814 this study.

	ABF	Dust	Smoke	Sea Salt
$\sigma$ (354 nm)	7.81	0.56	6.91	0.52
$\omega_o$ (354 nm)	1.0	0.88	0.85	1.0
$\sigma$ (388 nm)	6.96	0.58	6.07	0.52
$\omega_o$ (388 nm)	1.0	0.91	0.86	1.0

815

816



817 **Figure Captions**

818  
819 **Figure 1.** (a) Spatial distribution of NAAPS AODs, using NAAPS reanalysis data from the  
820 collocated OMI and NAAPS dataset for July 2007. (b). Simulated AI using NAAPS reanalysis  
821 data as shown in (a). (c). Spatial distribution of OMI AI using gridded OMI data from the  
822 collocated OMI and NAAPS dataset for July 2007. Grey color highlights those  $1 \times 1^\circ$   
823 (Latitude/Longitude) bins that have less than two collocated NAAPS and OMI AI data for the  
824 study period.

825 **Figure 2.** (a). Vertical distributions of smoke, dust, anthropogenic and sea salt aerosols for the test  
826 case as shown in (b). (b) Scatter plot of Jacobians of AI as a function of dust concentration: analytic  
827 versus finite difference solutions.

828 **Figure 3.** (a). Aqua MODIS true-color image over Central and North Africa for July 28, 2007.  
829 This composite was obtained from the NASA worldview site  
830 (<https://worldview.earthdata.nasa.gov/>). (b). Spatial distribution of Gridded OMI AI for 12 UTC,  
831 July 28, 2007. (c). Spatial distribution of NAAPS AOD from the NAAPS natural run for 12 UTC,  
832 July 28, 2007. (d). Similar to (c) but using NAAPS AOD from the AI-DA run. (e). Simulated AI  
833 using data from (c). (f). Simulated AI using data from (d).

834 **Figure 4.** (a). Spatial distribution of NAAPS AOD using NAAPS data from the AI-DA runs for  
835 July and August 2007. Only NAAPS data that have collocated OMI AI data are used. (b). Spatial  
836 distribution of simulated AI for July and August 2007 using NAAPS data from the AI-DA runs.  
837 (c). Spatial distribution of gridded OMI AI for July and August 2007. (d). Differences between  
838 Figures 4(b) and 4(c). (e-h) Similar to Figures 4(a)-4(d) but using NAAPS natural runs. Grey  
839 color highlights those  $1 \times 1^\circ$  (Latitude/Longitude) bins that have less than two collocated NAAPS  
840 and OMI AI data for the study period.



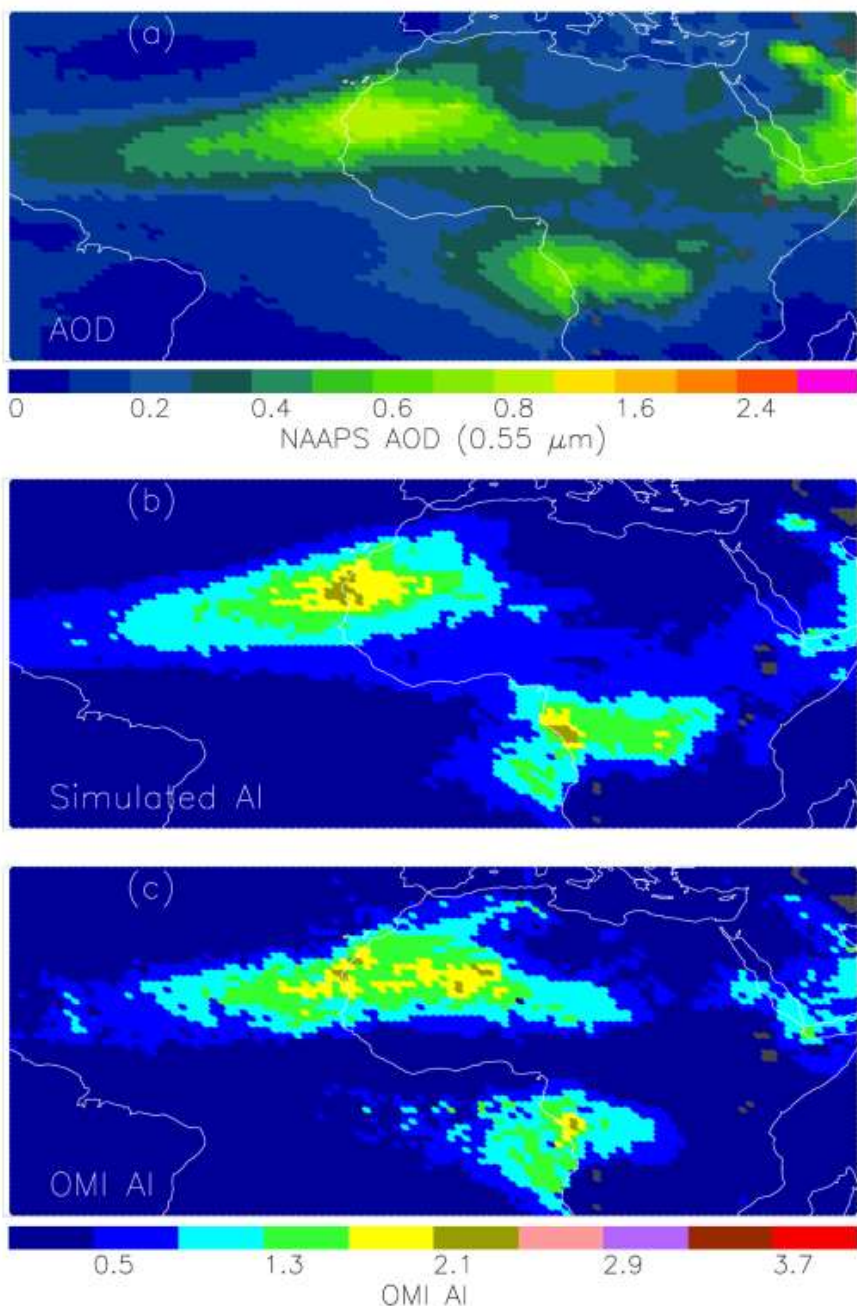
841 **Figure 5.** (a). Scatter plot of AERONET and NAAPS AOD (0.55  $\mu\text{m}$ ) using NAAPS data from  
842 the natural runs for July-August 2007 over the study region. (b). Similar to Figure 5(a) but using  
843 NAAPS data from the AI-DA runs. (c). Similar to Figure 5(a) but with AODs taken from the  
844 NAAPS reanalysis.

845 **Figure 6.** Spatial distributions of simulated AI at 12 Z on July 28, 2007 using NAAPS reanalysis  
846 data, with single scattering albedos of smoke aerosol at 354 and 388 nm taken to be: (a) 0.84 and  
847 0.84; (b) 0.85 and 0.85; (c) 0.86 and 0.86; (d) 0.85 and 0.85; (e) 0.85, 0.855; (f) 0.85 and 0.86.

848 **Figure 7.** (a). Vertical distributions of smoke and dust aerosol concentrations over 9.5°S and  
849 10.5°E at 12 Z on July 28, 2007 for both natural and AI DA runs. (b). Similar as (a) but over  
850 25.5°N and 12.5°W.

851

852



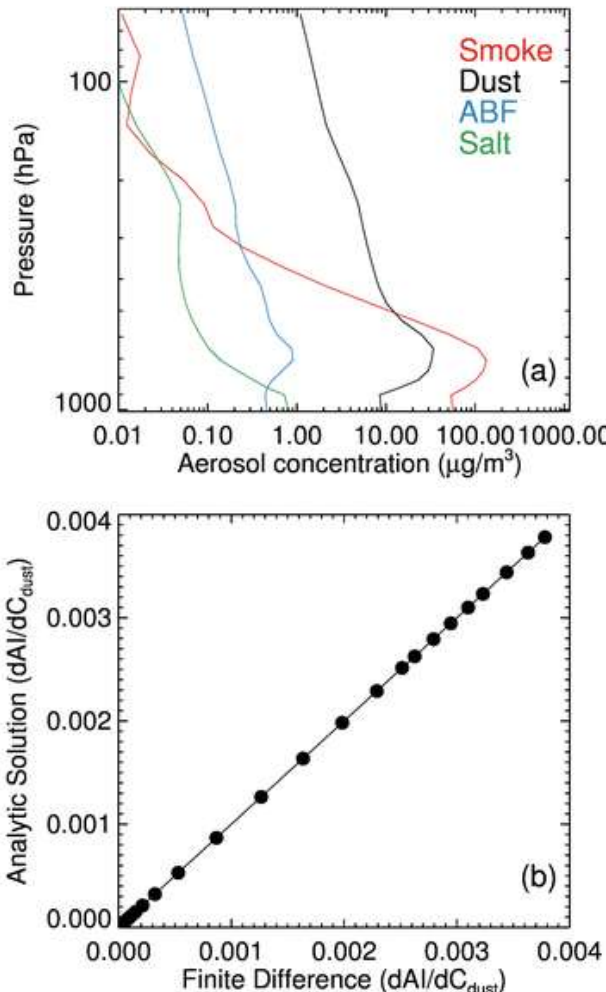
853

854

855 **Figure 1.** (a) Spatial distribution of NAAPS AODs, using NAAPS reanalysis data from the collocated OMI and NAAPS dataset for July 2007. (b). Simulated AI using NAAPS reanalysis data as shown in (a). (c). Spatial distribution of OMI AI using gridded OMI data from the collocated OMI and NAAPS dataset for July 2007. Grey color highlights those  $1 \times 1^\circ$  (Latitude/Longitude) bins that have less than two collocated NAAPS and OMI AI data for the study period.



856



857

858 **Figure 2.** (a). Vertical distributions of smoke, dust, anthropogenic and sea salt aerosols for the test  
859 case as shown in (b). (b) Scatter plot of Jacobians of AI as a function of dust concentration: analytic  
860 versus finite difference solutions.

861

862

863

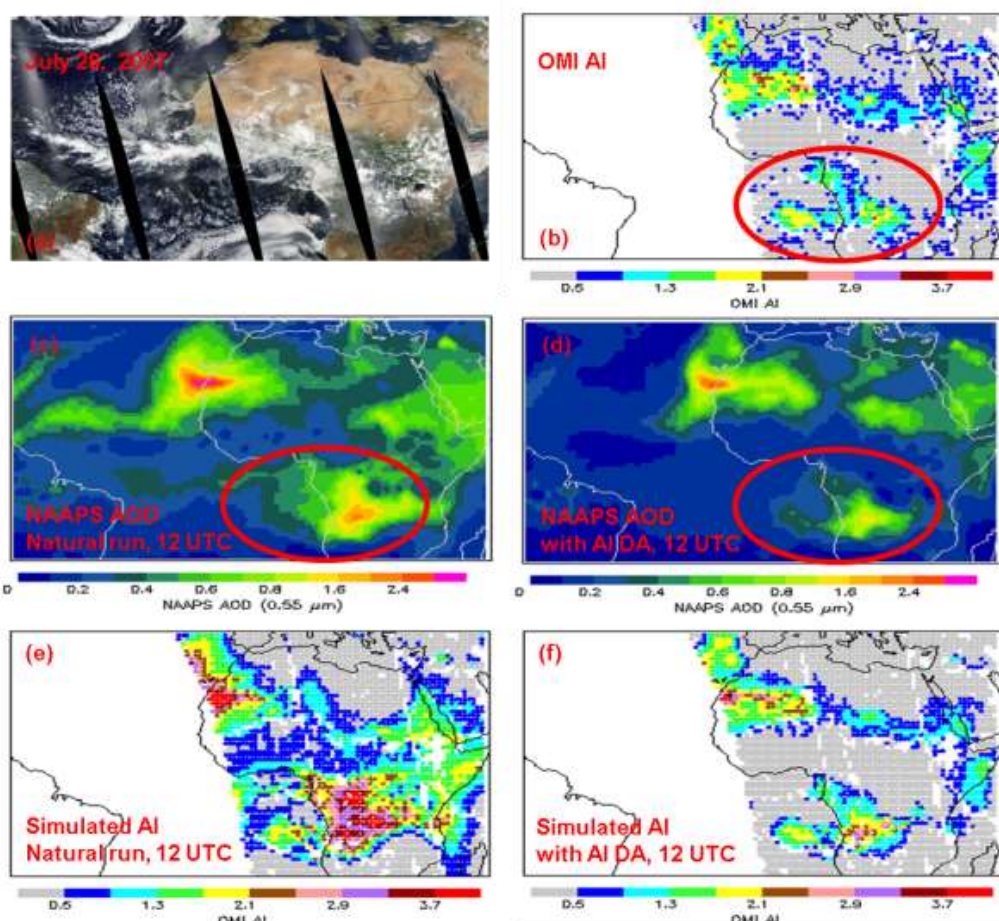
864

865



866

867



868

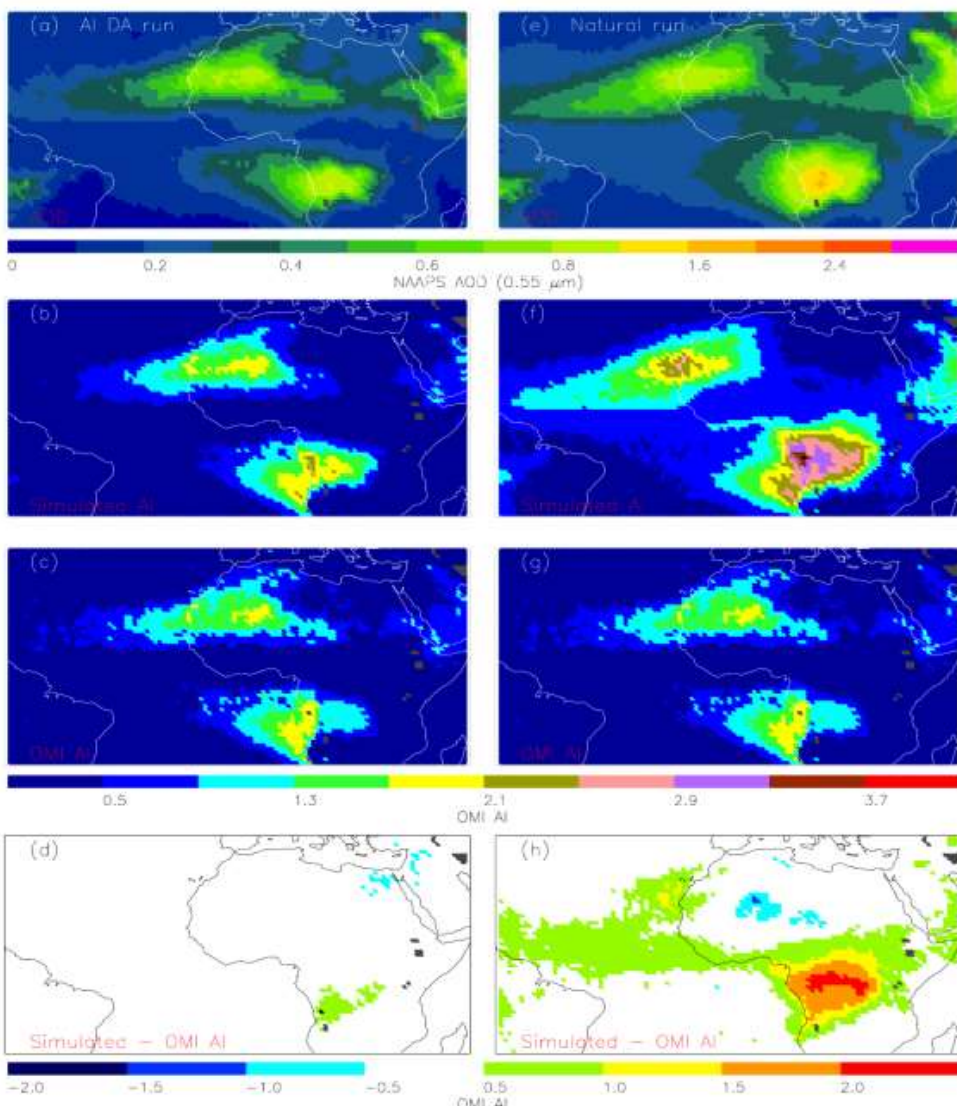
869 **Figure 3.** (a). Aqua MODIS true-color image over Central and North Africa for July 28, 2007.  
870 This composite was obtained from the NASA worldview site  
871 (<https://worldview.earthdata.nasa.gov/>). (b). Spatial distribution of Gridded OMI AI for 12 UTC,  
872 July 28, 2007. (c). Spatial distribution of NAAPS AOD from the NAAPS natural run for 12 UTC,  
873 July 28, 2007. (d). Similar to (c) but using NAAPS AOD from the AI-DA run. (e). Simulated AI  
874 using data from (c). (f). Simulated AI using data from (d).

875

876

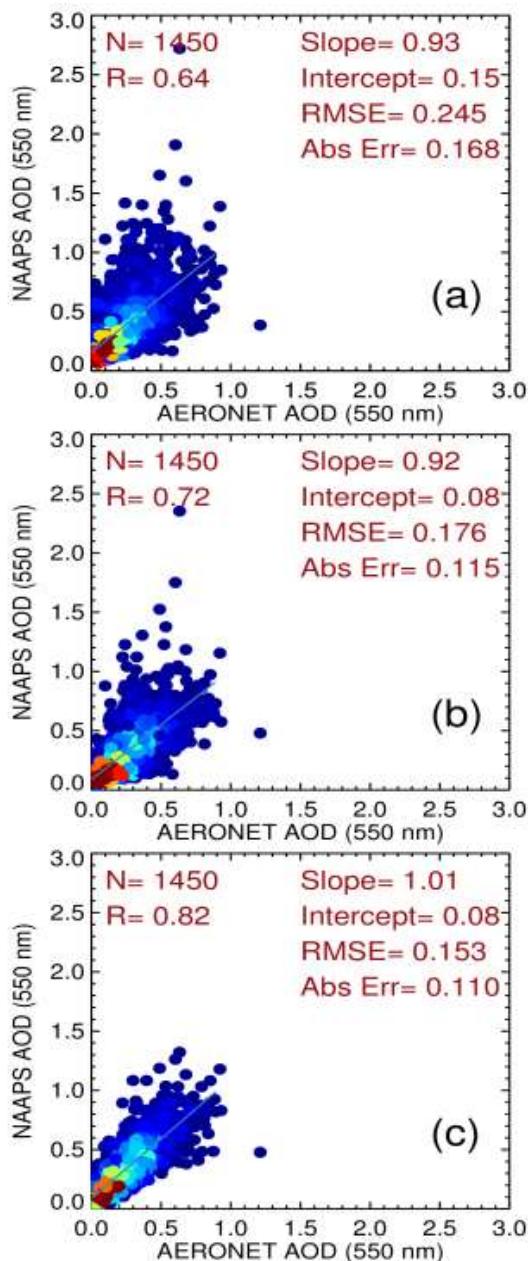
877

878



879

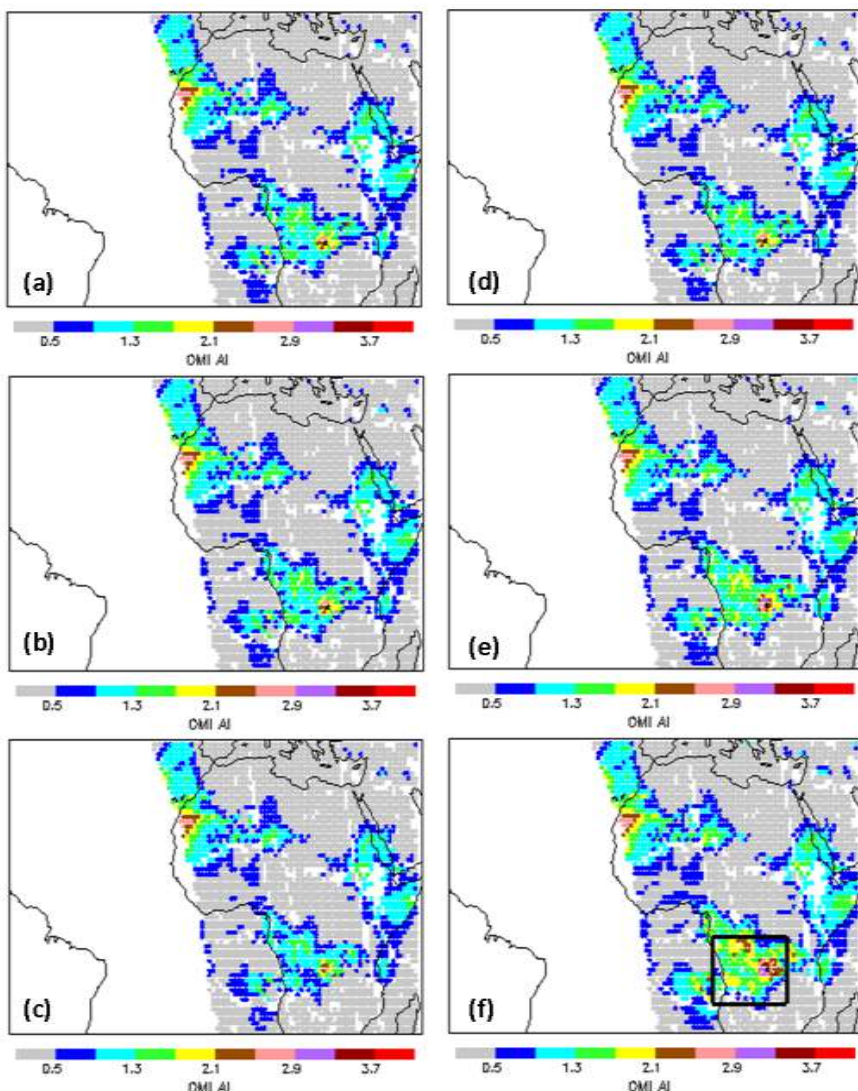
880 **Figure 4.** (a). Spatial distribution of NAAPS AOD using NAAPS data from the AI-DA runs for  
881 July and August 2007. Only NAAPS data that have collocated OMI AI data are used. (b). Spatial  
882 distribution of simulated AI for July and August 2007 using NAAPS data from the AI-DA runs.  
883 (c). Spatial distribution of gridded OMI AI for July and August 2007. (d). Differences between  
884 Figures 4(b) and 4(c). (e-h) Similar to Figures 4(a)-4(d) but using NAAPS natural runs. Grey  
885 color highlights those  $1 \times 1^\circ$  (Latitude/Longitude) bins that have less than two collocated NAAPS  
886 and OMI AI data for the study period.  
887



888

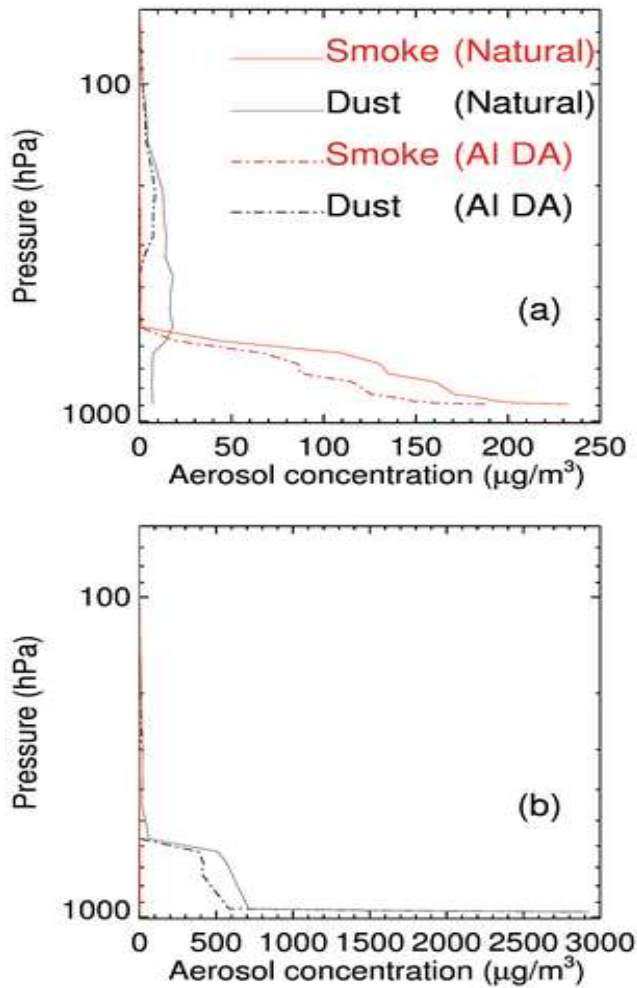
889 **Figure 5.** (a). Scatter plot of AERONET and NAAPS AOD (0.55  $\mu$ m) using NAAPS data from  
890 the natural runs for July-August 2007 over the study region. (b). Similar to Figure 5(a) but using  
891 NAAPS data from the AI-DA runs. (c). Similar to Figure 5(a) but with AODs taken from the  
892 NAAPS reanalysis.

893



894

895 **Figure 6.** Spatial distributions of simulated AI at 12 Z on July 28, 2007 using NAAPS reanalysis  
896 data, with single scattering albedos of smoke aerosol at 354 and 388 nm taken to be: (a) 0.84 and  
897 0.84; (b) 0.85 and 0.85; (c) 0.86 and 0.86; (d) 0.85 and 0.85; (e) 0.85, 0.855; (f) 0.85 and 0.86.  
898



899

900 **Figure 7.** (a). Vertical distributions of smoke and dust aerosol concentrations over 9.5°S and  
901 10.5°E at 12 Z on July 28, 2007 for both natural and AI DA runs. (b). Similar as (a) but over  
902 25.5°N and 12.5°W.

903

904